Classical dynamics of two-electron atoms near the triple collision

Min-Ho Lee,[1] Gregor Tanner,[2] and Nark Nyul Choi[1]
[1]*School of Natural Science, Kumoh National Institute of Technology, Kumi, Kyungbook 730-701, Korea*
[2]*School of Mathematical Sciences, University of Nottingham, University Park, Nottingham NG7 2RD, United Kingdom*
(Received 14 December 2004; published 24 May 2005)

The classical dynamics of two electrons in the Coulomb potential of an attractive nucleus is chaotic in large parts of the high-dimensional phase space. Quantum spectra of two-electron atoms, however, exhibit structures which clearly hint at the existence of approximate symmetries in this system. In a recent paper [Phys. Rev. Lett. **93**, 054302 (2004)], we presented a study of the dynamics near the triple collision as a first step towards uncovering the hidden regularity in the classical dynamics of two electron atoms. The nonregularizable triple collision singularity is a main source of chaos in three body Coulomb problems. Here, we will give a more detailed account of our findings based on a study of the global structure of the stable and unstable manifolds of the triple collision.

DOI: 10.1103/PhysRevE.71.056208 PACS number(s): 05.45.Mt, 45.50.−j, 34.10.+x

I. INTRODUCTION

Understanding the gravitational three-body problem as the simplest nontrivial many-body system is of prime importance when considering dynamical properties of the solar system such as its long term stability. Poincaré's proof of the nonintegrability of the three-body problem in 1890 showed that closed form solutions of many-body systems are the exception rather than the rule. This insight stood at the beginning of modern dynamical systems theory concerned with developing tools to understand the structures and stability properties of nonlinear dynamics. Still, more than one hundred years later, we know remarkably little about the dynamics of three-body problems due to the large dimensionality of the system, the long range interactions and the complexity of the dynamics near the non-regularizable triple collision; see [1], for a well written account of the history of celestial dynamics before and after Poincaré's discovery.

The microscopic counterpart of planetary motion, the dynamics of electrically charged particles, occurs naturally in atoms and molecules; it has thus mainly been studied in the context of quantum mechanics. First attempts to analyze the classical dynamics of many-body Coulomb systems such as two-electron atoms have been undertaken by the founding fathers of quantum mechanics in order to extend Bohr's hydrogen quantization rules to more complex atoms. The failure to do so and the discovery of Schrödinger's equation brought this project to an abrupt halt in 1925. Only a better understanding of the use of semiclassical methods for nonintegrable systems pioneered by Gutzwiller and others [2] in the 1970's brought three-body Coulomb systems back onto the agenda. These efforts led to the successful semiclassical description of parts of the helium spectra in terms of collinear subspaces of the full three-body problem in the 1990's [3,4]. Surprising regularities and selection rules in the spectrum of two electron atoms, which have puzzled atomic physicists for decades, could now be explained in terms of stability properties of an underlying classical dynamics; see the review [5] for more details.

Advances in a semiclassical treatment of the three-body Coulomb problems were possible only due to a better understanding of the classical dynamics in these systems. The existence of a perfect Smale horseshoe giving rise to a complete binary symbolic dynamics were uncovered for the collinear configuration where the two electrons are on different sides of the nucleus (the *eZe* configuration) [3,5–8]. Such a behavior is a rare feature in physically relevant dynamical systems and is here intricately linked to the presence of the nonregularizable triple collision. The collinear phase space where both electrons stay on the same side of the nucleus—the *Zee* configuration—has been found to be largely stable in the full 5 dimensional phase space for $1<Z<10$ [4,5,9].

Studies of the dynamics beyond the collinear configurations have so far remained rare [10,11]. Quantum mechanical calculations [12,13] suggest, however, that two-electron atoms have a variety of approximate symmetries which express themselves in the form of approximate quantum numbers in spectra of these atoms. This has been explained qualitatively by group theoretical arguments [12] and in terms of adiabatic invariants [14], see [5] for an overview. It is thus only natural to ask how the existence of such approximate symmetries is reflected in the classical dynamics of the corresponding three-body Coulomb problem.

Recently, we presented an analysis of the classical dynamics near the triple collision in two-electron atoms in the full $L=0$ phase space [15]. The triple collision and associate collision manifolds are the key in understanding the structure of the dynamics of the 5-dimensional phase space. Here, we will give a more detailed account of the surprising effects observed in classical scattering signals below the three particle breakup energy as well as how these effects arise due to the topology of the phase space and the particle exchange symmetry.

The paper is organized as follows: in Sec. II we introduce the McGehee scaling technique in hyperspherical coordinates. In Sec. III, we describe the structure of the collision manifolds in the phase space for $E=0$ which turns out to be relatively simple. We then treat the dynamics near the triple collision for $E<0$ in Sec. IV and we present scaling laws similar to Wannier's threshold law [16] in some detail. In the Appendix, we give the equations of motions combining Kustaanheimo-Stiefel transformation with McGehee scaling

and discuss the properties of a specific surface of section used in the main text.

II. EQUATIONS OF MOTION

The classical three-body system can be reduced to four degrees of freedom after eliminating the center of mass motion and incorporating the conservation of the total angular momentum. We will focus here on the special case of zero angular momentum, for which the motion of the three particles is confined to a plane fixed in configuration space [17] and the problem reduces to three degrees of freedom, that is, a five dimensional phase space for fixed energy. We will as usual work in the infinite nucleus mass approximation; the Hamiltonian including finite nuclear mass terms can be found in [7,8]. In the following we will use scaling properties in the three body Coulomb problem in two different ways: first, by scaling the phase space coordinates with respect to energy and, second, by scaling out an overall size parameter thus considering only the shape dynamics of the system.

By choosing a scaling transformation with respect to the total energy E according to

$$\mathbf{r}_i = |E|\mathbf{r}'_i, \quad \mathbf{p}_i = \frac{1}{\sqrt{|E|}}\mathbf{p}'_i, \tag{1}$$

where $\mathbf{r}_i$, $\mathbf{p}_i$ refer to the new coordinates and momenta of electron $i=1$ or 2, respectively, and introducing a time transformation

$$t = \sqrt{|E|^3}t', \tag{2}$$

one deduces the new equations of motion from the Hamiltonian

$$H = \frac{\mathbf{p}_1^2}{2} + \frac{\mathbf{p}_2^2}{2} - \frac{Z}{r_1} - \frac{Z}{r_2} + \frac{1}{r_{12}} = \begin{cases} +1: & E > 0, \\ 0: & E = 0, \\ -1: & E < 0. \end{cases} \tag{3}$$

Here, Z refers to the charge of the nucleus (in units of the elementary charge) and masses are given in units of the mass of the electron. We will in general consider $Z=2$, that is, helium, if not specified otherwise. Furthermore, r_i, r_{12} denotes the nucleus-electron and electron-electron distances, respectively.

From Eq. (3) it is clear that we only have to consider three different values of the energy. Our ultimate goal is to better understand the bound and resonance states in quantum two-electron atoms and we are thus most interested in the classical dynamics for $E<0$, that is, we will consider $E=-1$. In this regime, only one electron can escape classically and it will do so for most initial conditions. It turns out, however, that one can learn a lot about the $E<0$—dynamics by analyzing the dynamics at the three-particle breakup threshold $E=0$ in detail. The phase space can be reduced to 4 dimensions in this case and the dynamics in the reduced space turns out to be relatively simple as will be discussed in Sec. III. A similar approach has been employed by Wannier [16]; by extrapolating dynamical behavior at $E=0$ to the dynamics for $E>0$, he was able to deduce his celebrated threshold law for the total two-electron ionization cross section which turns out to be completely classical in nature [18].

How are the spaces $E=\pm 1$ and $E=0$ connected? When considering scattering trajectories where one electron, say electron 1, approaches the nucleus from $r_1=\infty$ with energy E_1, the energy scaling property, Eqs. (1) and (2), implies that the dynamics depends on the ratio E/E_1 only rather than on the absolute values of E and E_1 separately. The limit $E\to 0$ is thus equivalent to $E/E_1\to 0$ which can for fixed $E=E_1+E_2=\pm 1$ be achieved by for example considering the limit $E_1\to\infty$. (In the same way, we may consider the limit $E\to 0$ for fixed E_1.) As we will see in Sec. IV, the limit $E\to 0$ is also closely related to the dynamics near the triple collision.

The dynamics for $E=0$ can be reduced to 4 dimension using an additional scaling relation. Following McGehee [19], one uses the similarity of the overall dynamics when rescaling the total size of the system. This means that the shape dynamics given by the relative positions of the three particles in space decouples from the overall change in size of the system in certain limits. We introduce the hyperradius $R=\sqrt{r_1^2+r_2^2}$ as an overall scaling parameter and shape parameters given by the hyperangle $\alpha=\tan^{-1}(r_2/r_1)$ and the interelectronic angle $\theta=\angle(\mathbf{r}_1,\mathbf{r}_2)=\theta_1-\theta_2$ with θ_i being the azimuthal angles. The Hamiltonian (3) written in these hyperspherical coordinates has for angular momentum $L=0$ the form

$$\begin{aligned} H &= \frac{1}{2}\left(p_{r_1}^2 + \frac{p_{\theta_1}^2}{r_1^2} + p_{r_2}^2 + \frac{p_{\theta_2}^2}{r_2^2}\right) + \frac{1}{R}V(\alpha,\theta) \\ &= \frac{1}{2}\left(p_R^2 + \frac{p_\alpha^2}{R^2} + \frac{p_\theta^2}{R^2\cos^2\alpha\sin^2\alpha}\right) + \frac{1}{R}V(\alpha,\theta), \end{aligned} \tag{4}$$

with

$$V(\alpha,\theta) = -\frac{Z}{\cos\alpha} - \frac{Z}{\sin\alpha} + \frac{1}{\sqrt{1-2\cos\alpha\sin\alpha\cos\theta}}.$$

Note, that for $L=0$, we have

$$p_\theta = p_{\theta_1} = -p_{\theta_2}, \tag{5}$$

where p_θ is the momentum conjugate to the interelectronic angle θ. The triple collision corresponds to $R=0$, here. For Hamiltonians of the form (4), one can separate the shape dynamics from the overall scale dynamics given by the time dependence of the hyperradius $R(t)$. Such a separation is exact for $E=0$ and reflects the dynamics in the limit $R\to 0$, that is, close to the triple collision for $E\neq 0$. In analogy with (1) and (2), one defines the (time-dependent) scaling transformation

$$\bar{\alpha} = \alpha, \quad \bar{\theta} = \theta, \quad \bar{R} = \frac{1}{R}R = 1,$$

$$\bar{p_R} = \sqrt{R}p_R, \quad \bar{p_\alpha} = \frac{1}{\sqrt{R}}p_\alpha, \quad \bar{p_\theta} = \frac{1}{\sqrt{R}}p_\theta,$$

$$d\bar{t} = \frac{1}{R^{3/2}} dt, \quad \bar{H} = \bar{E} = RE. \tag{6}$$

Note that the above transformations are invariant under rescaling the energy according to (1) and (2), that is, it is again sufficient to consider the case $E = \pm 1$ or 0 only. The transformations (6) do, however, destroy the symplectic structure of the original differential equations; the new Hamiltonian $\bar{H}$ is in particular no longer a constant of motion for $E \neq 0$. The equations of motion with respect to the rescaled time are

$$\dot{\alpha} = p_\alpha, \quad \dot{p}_\alpha = -\frac{1}{2} p_R p_\alpha + p_\theta^2 \frac{\cos^2\alpha - \sin^2\alpha}{\sin^3\alpha \cos^3\alpha} - \frac{\partial}{\partial\alpha} V(\alpha, \theta),$$

$$\dot{\theta} = \frac{p_\theta}{\sin^2\alpha \cos^2\alpha}, \quad \dot{p}_\theta = -\frac{1}{2} p_R p_\theta - \frac{\partial}{\partial\theta} V(\alpha, \theta),$$

$$\dot{\bar{H}} = p_R \bar{H}, \quad \dot{p}_R = \frac{1}{2} p_\alpha^2 + \frac{1}{2} \frac{p_\theta^2}{\cos^2\alpha \sin^2\alpha} + \bar{H}, \tag{7}$$

with

$$\bar{H} = RH = \frac{1}{2}\left(p_R^2 + p_\alpha^2 + \frac{p_\theta^2}{\cos^2\alpha \sin^2\alpha} \right) + V(\alpha, \theta) = RE, \tag{8}$$

where we skip the bar signs again for convenience except for $\bar{H}$.

The new equations of motion (7) are indeed independent of R; the explicit time dependence of $R(t)$ can be recovered from (8) for $E \neq 0$ or may be obtained by integrating $\dot{R} = p_R R$ along a trajectory for $E = 0$.

The problem simplifies when considering the special initial condition $\bar{H} = 0$, that is, $E = 0$ *or* $R = 0$. First, a true reduction in dimensionality is achieved as $\bar{H}$ becomes a constant of motion and we are left with only four independent coordinates. Secondly, for $\bar{H} = 0$ we have $\dot{p}_R \geqslant 0$, and the scaled momentum p_R increases monotonically with time. This leads to a relatively simple overall dynamics in the $\bar{H} = 0$ subspace which will be studied in detail in the next section.

The triple collision itself has been lifted from the equations of motions (7) by the time transformation in (6). Two fixed points are created instead which are related to the triple collision. These fixed points cannot be reached in finite (scaled) time which is a manifestation of the nonregularizability of the triple collision singularity. Other singularities are still present in (7), the binary collisions at $r_i = 0$ or equivalently at $\alpha = 0$ or $\pi/2$. They can be regularized by standard techniques such as Kustaanheimo-Stiefel (KS) transformation [8,23,24]. A set of singularity-free equations of motions is obtained by first employing a KS transformation using parabolic coordinates and then using McGehee's scaling technique for this new set of coordinates. Details of the derivation can be found in Appendix A; the resulting differential equations (A7), (A11), and (A14) have been used throughout the paper for numerical calculations. The description in terms of parabolic coordinates is, however, less transparent than the hyperspherical coordinates and the latter are thus used in the discussion of the dynamics.

At the binary collisions $\alpha = 0$ or $\alpha = \pi/2$, the value of p_α makes an instantaneous transition from $\mp\infty$ to $\pm\infty$ whereas all other variables behave smoothly at these points. We may thus identify p_α before and after the collision by introducing the regularized variable

$$\bar{p}_\alpha = p_\alpha \sin 2\alpha. \tag{9}$$

The resulting set of smooth hyperspherical coordinates including the regularized $\bar{p}_\alpha$ will be used in our description of the phase space structures. Note, however, that in contrast to the case of the collinear *eZe* subspace [6,7,19], (9) cannot be used to remove the binary collision singularities in the equations of motions. Instead, one has to go to parabolic coordinates to obtain a set of fully regularized ODE's as presented in Appendix A.

III. DYNAMICS FOR $E = 0$

A. Fixed points and invariant subspaces

In order to understand the dynamics near the triple collision for $E < 0$ it is advantageous to analyse the topology of the flow generated by (7) for $E = 0$. We start by briefly discussing the fixed points and the invariant subspaces of the dynamics in the rescaled coordinates. For $E = 0$, the dynamics takes place on a 4-dimensional manifold in a 5- dimensional space. There are two fixed points of the flow, that is,

$$\alpha = \pi/4, \quad \theta = \pi, \quad p_\alpha = 0, \quad p_\theta = 0,$$
$$p_R = \pm\sqrt{\sqrt{2}(4Z - 1)} = \pm P_0.$$

These fixed points correspond to trajectories in the full phase space where both electrons fall into the nucleus symmetrically along the collinear axis, that is, the *triple collision point* (TCP) with $p_R = -P_0$ and its time reversed partner, the trajectory of symmetric double escape, that is, the *double escape point* (DEP) with $p_R = P_0$. In addition, there are three invariant subspaces: the collinear spaces $\theta = \pi$, $p_\theta = 0$ (the *eZe* configuration) and $\theta = 0$, $p_\theta = 0$ (the *Zee* configuration) and the so-called Wannier ridge (WR) of symmetric electron dynamics with $\alpha = \pi/4$, $p_\alpha = 0$.

In the *eZe* space with Hamiltonian

$$\bar{H} = \frac{1}{2}(p_R^2 + p_\alpha^2) - \frac{Z}{\cos\alpha} - \frac{Z}{\sin\alpha} + \frac{1}{\cos\alpha + \sin\alpha} = 0, \tag{10}$$

a typical trajectory represents an outer electron coming from infinity with $p_R = -\infty$, $\alpha = 0$ or $\pi/2$ and one of the two electrons leaving towards infinity with $p_R \to \infty$, $\alpha \to 0$ or $\pi/2$. Identifying the points $p_\alpha = \pm\infty$ at the binary collisions $\alpha = 0$, $\pi/2$ by using $\bar{p}_\alpha$ as discussed in Sec. II, the topology of the *eZe*—phase space takes on the form of a sphere with four points taken to infinity; see Fig. 1(a) [6,7,19]. The two fixed points are located at the saddles between the arms stretching in forward and backward directions along the p_R axis. The *eZe*-space for $E < 0$ fills the interior of the manifold in Fig. 1(a).

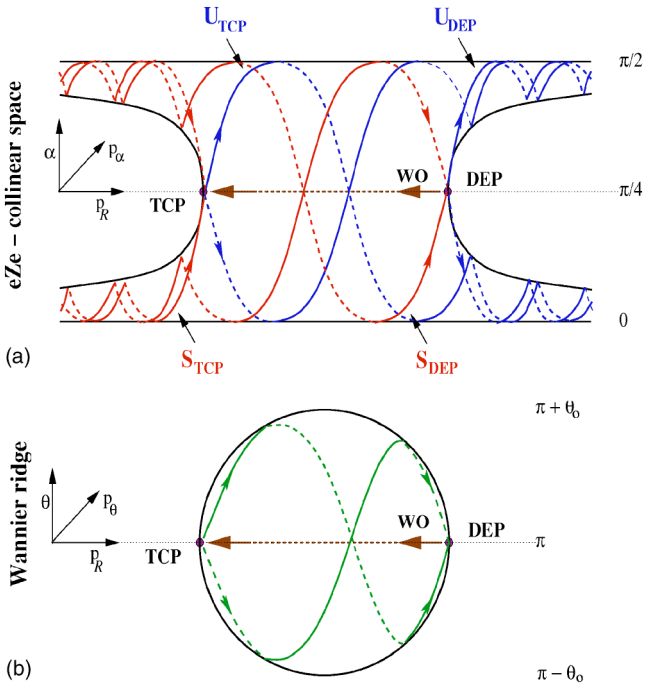

FIG. 1. (Color online) The *eZe* manifold (a) and the Wannier ridge manifold (b) for $E=0$. The angle θ_0 in (b) corresponds to the maximal deviation from the collinear configuration $\theta=\pi$ possible in the WR for $E=0$ [in fact $\pi-\theta_0=\arccos(1-1/8Z^2)$]. The two-dimensional invariant subspaces are embedded in the full phase space $E\leqslant 0$ of dimension 5; the subspaces are connected at the TCP and DEP (for $E=0$) and along the Wannier orbit (WO) for $E<0$.

The Wannier ridge space described by

$$\bar{H}=\frac{1}{2}p_R^2+2p_\theta^2-2\sqrt{2}Z+\frac{1}{\sqrt{1-\cos\theta}}=0 \tag{11}$$

is, on the other hand, a compact space with the topology of a sphere where the fixed points form opposite poles; see Fig. 1(b). The dynamics for $E=0$ is trivial as the full space acts as the unstable manifold of the TCP as well as the stable manifold of the DEP. The interior of the sphere corresponds to the phase space of the WR for $E<0$. The dynamics is of mixed type containing stable islands and ergodic regions for $Z>1/4$. In what follows we will not discuss the features of the WR dynamics in more detail, see [5,21] for details as well as [22] for a more rigorous approach. Note, that the *eZe* configuration and the WR are connected at the fixed points (in $E=0$) and along the so-called Wannier orbit (WO) or symmetric stretch orbit with $\alpha=\pi/4$, $\theta=\pi$, $p_\alpha=0$ and $p_\theta=0$ with $E<0$.

The overall dynamics is invariant under the transformation $p_j\rightarrow -p_j$ and $dt\rightarrow -dt$ with $j=R,\theta$ or α reflecting the time-reversal symmetry of the original problem. The triple collision point and double escape point are thus equivalent and related by time reversal symmetry.

The linearized dynamics near the fixed points can be obtained directly from Eqs. (7); for each fixed point, two of the four eigenvectors in $E=0$ lie in the *eZe* space, the other two on the Wannier ridge. One obtains in particular for the eigenvalues at the TCP [16]

$$\lambda_{S_T}^{eZe}=\frac{P_0}{4}\left(1-\sqrt{\frac{100Z-9}{4Z-1}}\right)\quad eZe\text{: stable},$$

$$\lambda_{U_T}^{eZe}=\frac{P_0}{4}\left(1+\sqrt{\frac{100Z-9}{4Z-1}}\right)\quad eZe\text{: unstable},$$

$$\lambda_{U_T}^{WR}=\frac{P_0}{4}\left(1\pm\sqrt{\frac{4Z-9}{4Z-1}}\right)\quad \text{Wannier ridge: unstable}, \tag{12}$$

and for the DEP

$$\lambda_{U_D}^{eZe}=-\frac{P_0}{4}\left(1-\sqrt{\frac{100Z-9}{4Z-1}}\right)\ eZe\text{: unstable},$$

$$\lambda_{S_D}^{eZe}=-\frac{P_0}{4}\left(1+\sqrt{\frac{100Z-9}{4Z-1}}\right)\ eZe\text{: stable},$$

$$\lambda_{S_D}^{WR}=-\frac{P_0}{4}\left(1\pm\sqrt{\frac{4Z-9}{4Z-1}}\right)\ \text{Wannier ridge: stable}. \tag{13}$$

The eigendirections leading out of the $\bar{H}=0$ subspace are directed along the p_R axis; the corresponding stable and unstable manifolds $S_T^{H\neq 0}$, $U_D^{H\neq 0}$ are embedded both in the *eZe* and WR space and are thus identical to the Wannier orbit. That is, the WO forms a heteroclinic connection leading from the DEP to the TCP. The stabilities along the eigendirections are

$$\lambda_{S_T}^{\bar{H}\neq 0}=-P_0,\quad \lambda_{U_D}^{\bar{H}\neq 0}=P_0, \tag{14}$$

where $P_0=\sqrt{\sqrt{2}(4Z-1)}$ as defined above.

Table I gives an overview over how various parts of the stable and unstable manifold of the fixed points are embedded within the invariant subspaces. The TCP has, in particular, three unstable directions and two stable directions of which one is coming from outside the $E=0$ subspace; see also Fig. 1. The converse holds for the DEP which has three stable directions all in $E=0$ and two unstable directions.

The TCP can only be reached by trajectories on the 2-dimensional stable manifold of the TCP which is fully embedded in the *eZe* space; see Fig. 1(a). Trajectories in $E=0$ approaching the TCP in the *eZe* space close to the S_T^{eZe} will leave the neighborhood of the TCP along the unstable manifold U_T^{eZe} which leads to single ionization of one of the electrons eventually. The dynamics near the TCP is thus for $E=0$ well separated from the DEP and the two fixed points are dynamically not connected. (Strictly speaking, this is true only for $Z>0.287742\ldots$; at the critical value the system is degenerate, that is, U_T^{eZe} coincides with S_D^{eZe} [6]; this parameter regime is, however, physically not relevant.)

The situation changes when leaving the *eZe* space into the full 4-dimensional space $E=0$. The Wannier ridge itself pro-

TABLE I. Dimensions and embedding spaces of invariant subspaces of the stable or unstable manifolds of the fixed points TCP and DEP.

	S_T^{eZe}	$S_T^{\bar{H}\neq 0}$	U_T^{eZe}	U_T^{WR}	S_D^{eZe}	S_D^{WR}	U_D^{eZe}	$U_D^{\bar{H}\neq 0}$	S_T	U_T	S_D	U_D
Dimension	1	1	1	2	1	2	1	1	2	3	3	2
Embedded in	*eZe*	*eZe*	*eZe*		*eZe*		*eZe*	*eZe*	*eZe*			*eZe*
		WR		*WR*		*WR*		*WR*				
	$\bar{H}=0$	$\bar{H}\neq 0$	$\bar{H}=0$	$\bar{H}=0$	$\bar{H}=0$	$\bar{H}=0$	$\bar{H}=0$	$\bar{H}\neq 0$		$\bar{H}=0$	$\bar{H}=0$	

vides now a connection between the TCP and DEP and trajectories approaching the TCP can leave along the Wannier ridge and thus come close to the DEP. The 3-dimensional stable manifold S_D of the DEP which contains the Wannier ridge and the S_D^{eZe} acts in fact as the stable manifold of the Wannier ridge itself or more precisely $S_{WR}=S_D\cup S_T^{eZe}$ and S_D is thus connected to S_T^{eZe}. In what follows, the S_D will be of special importance for understanding some of the striking features in the classical electron-impact scattering signal found for $E=0$; see Sec. III C, as well as in the $E<0$ regime discussed in detail in Sec. IV.

A summary of the submanifolds of the stable and unstable manifolds of the fixed points and the spaces they are embedded in can be found in Table I. Note in particular that U_T and U_D are related to S_D and S_T by time reversal symmetry; thus, U_T together with U_D^{eZe} form the unstable manifold of the Wannier ridge, U_{WR}, in $E=0$.

B. The stable manifold of the DEP

We analyze first the topology of the 4-dimensional invariant subspace $\bar{H}=0$ which is most conveniently studied by considering the 3-dimensional Poincaré surface of section (PSOS) $\theta=\pi$, $\dot{\theta}\geqslant 0$ in α-$\bar{p}_\alpha$-p_R coordinates. The surface $\theta=\pi$ is indeed a good PSOS in the sense that the flow is not tangential to the surface except for trajectories in the *eZe* space which is an invariant subspace fully embedded in the PSOS; the *eZe* forms in fact the boundary of the surface of section as can be seen from Eqs. (8) and (10). In addition, almost all trajectories cross the surface at least once; see Appendix B for details.

The PSOS has in α-$\bar{p}_\alpha$-p_R coordinates the form of the *eZe* space in Fig. 1(a). The interior of the 2-dimensional *eZe* manifold represents here, however, the domain of the Poincaré map $\theta=\pi$ for $p_\theta\geqslant 0$ and $E=0$; see Fig. 2. The fixed points TCP and DEP lie on the boundary of the PSOS, whereas the 2-dimensional Wannier ridge space in the PSOS forms a line connecting the TCP and DEP along the p_R axis at $\alpha=\pi/4$, $p_\alpha=0$.

Due to $\dot{p}_R\geqslant 0$ in (7), p_R increases monotonically with time leading to a relatively simple overall dynamics in $\bar{H}=0$. Its important features can be characterized by the behavior of the stable or unstable manifolds of the fixed points. Especially, the codimension one manifold S_D is a good candidate for supplying a dividing surface in the full $E=0$ phase space. In Fig. 2, the topology of the S_D in the PSOS is discussed by showing cuts through the PSOS at fixed p_R values with $p_R<P_0$.

The S_D is for $-P_0\leqslant p_R\leqslant P_0$ bounded by the 1-dimensional stable manifold S_D^{eZe} in the *eZe* space, and the 2-dimensional Wannier ridge. Remarkable is the evolution of this manifold near the TCP at $p_R=-P_0$, where the phase space itself splits into two distinct parts. Starting at the DEP fixed point at $p_R=P_0$, we will discuss the form of S_D by going towards decreasing p_R values which corresponds essentially to an evolution of the S_D backward in time. The S_D undergoes the usual stretching and folding mechanism typical for an unstable manifold in bounded domains. The stretching and folding is here facilitated by an overall rotation of the space around the Wannier ridge axis $\alpha=\pi/4$, $p_\alpha=0$ and a certain "stickiness" near $\alpha=0$ or $\pi/2$ (see the cuts B and C in Fig. 2). The behavior near the binary collision points is due to our choice of regularized momentum $\bar{p}_\alpha$ which projects the phase space at $\alpha=0$ or $\pi/2$ onto the point $\bar{p}_\alpha=0$.

As p_R moves towards the TCP at $-P_0$, the phase space develops a bottleneck whereas the S_D stretches over the whole phase space 5 times by now. That means, that as p_R

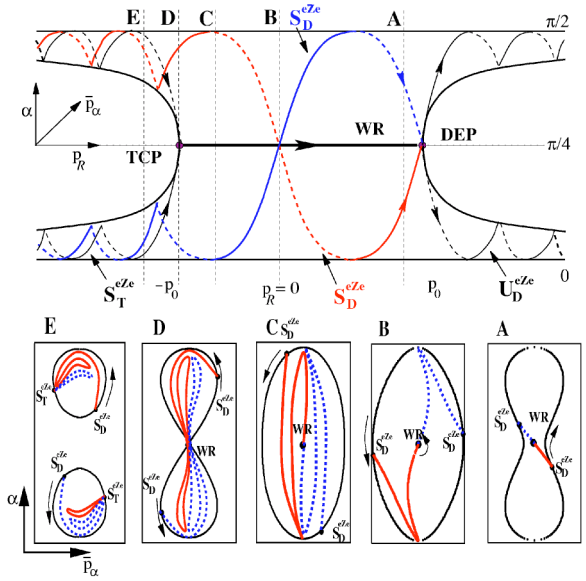

FIG. 2. (Color online) The PSOS $\theta=\pi$ in the $E=0$ subspace in α-$\bar{p}_\alpha$-p_R coordinates. The *eZe* space forms the boundary of the PSOS; the WR connects the TCP and DEP along the p_R axis at $\alpha=\pi/4$, $p_\alpha=0$. Various cuts of the PSOS at fixed p_R values together with the S_D are shown below. The two arms of the S_D stretching from the WR towards the S_D^{eZe} on the *eZe* boundary are shown as full and dashed line, respectively. (The cuts C–E are drawn schematically to enhance important features.)

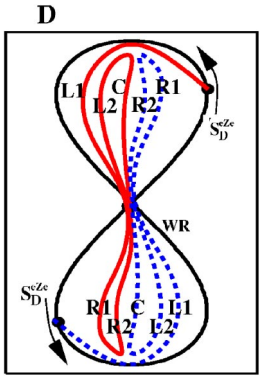

FIG. 3. (Color online) The 5 pieces of the S_D at the cut D in Fig. 2 are labeled $R1$, $R2$, C, $L2$, and $L1$ as indicated in the figure.

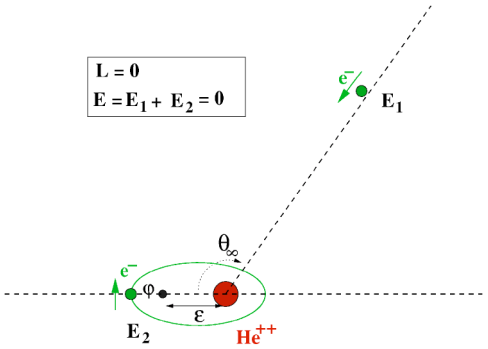

FIG. 4. (Color online) Parametrization of three-body Coulomb dynamics as a scattering problem.

decreases further passing through $-P_0$, the S_D is cut at the TCP into distinct parts; see D in Fig. 2. We end up with 5 pieces of the S_D in each arm. The only way to leave the TCP (backward in time) is along the stable manifold S_T^{eZe} in the *eZe* space. This implies that the 5 pieces in each arm are connected at the S_T^{eZe} for $p_R<-P_0$ forming two loops and one connection to the *eZe* boundary at S_D^{eZe}, see Fig. 2(e). The S_T^{eZe} itself is thus a boundary of the S_D without being a part of it and S_D connects the stable manifolds S_T^{eZe} and S_D^{eZe} for $p_R<-P_0$.

There are two main routes to approach the DEP for electrons coming in from $p_R=-\infty$ close to the *eZe* boundary: first, a trajectory can approach the DEP "directly" by moving in the vicinity of the S_D^{eZe}; this is the only path open in the *eZe* space. In the full $E=0$ space, a second route opens up; trajectories close to the S_T^{eZe} approaching the TCP can stay close to one of the 5 leaves of the S_D and move along the S_D toward the DEP. This twofold approach turns out to be the main new element when moving away from the collinear spaces. For later reference, we will label the leaves of the S_D according to $R1$, $R2$, C, $L2$ and $L1$ as indicated in Fig. 3. Note that the central leaf (C) is the one connected directly to the WR for $p_R>-P_0$, whereas the leaves to the right, $R_{1,2}$, and to the left, $L_{1,2}$, do not stay close to the WR when leaving the TCP.

Figure 2 is based on numerical calculations for $Z=2$; no changes in the topological structure and in the number of leaves of the S_D are recorded for nuclear charges Z in the range $1\leqslant Z\leqslant 10$. Note that the stability exponents are about 5 times larger in the *eZe* space than those in the WR; thus, trajectories approaching the DEP will do so in general along the Wannier ridge space.

C. Scattering signal for $E=0$

The phase space dynamics for $E=0$ is relatively simple; the condition $\dot{p}_R\geqslant 0$ ensures in particular that the DEP and TCP are the only fixed points and there are no periodic orbits and thus no chaos. We will discuss in this section scattering signals for the $E=0$ space in some detail and interpret them on the basis of the phase space structure presented above. This will be helpful when turning to the much more complex dynamics for $E<0$ which will be investigated in the form of a scattering problem in Sec. IV.

A set of suitable parameters fully determining the initial conditions of a scattering trajectory at energy $E=0$ and $L=0$ are shown in Fig. 4; these are in particular the angle θ_∞ measuring the angle between the major axis of the Kepler ellipse of the inner electron and the incoming direction of the outer electron, the eccentricity e of the ellipse and the angle variable φ of the action-angle variable pair of the inner electron at time $t=0$. The dynamics at $E=0$ is invariant under changing the initial energy E_1 of electron 1 up to a scaling transformation as $E/E_1=0$ independent of E_1; we thus fix the $E_1=1$. For $e=1$ (degenerate ellipse), θ_∞ coincides with the inter-electronic angle θ used in the hyperspherical coordinates. The angular momentum of the incoming electron is determined by the eccentricity e and chosen such that the total angular momentum $L=0$. For numerical purposes, we start the incoming electron at $r_1=50Z$ and we compute the trajectory until the outgoing electron reaches $r_i=500Z$, $i=1$ or 2.

1. The eZe configuration

We start with the simple case—scattering in the collinear *eZe* space—for which the dynamics takes place on the boundary of the PSOS, see Fig. 2. In Fig. 5, we record the scattering time (a) and energy of the outgoing electron (b) as a function of the phase angle φ. The initial conditions roughly coincide with a cut through the *eZe* manifold at $p_R=\text{const}\ll -P_0$. Note also that the scattering time is plotted here in real time, not in the scaled time used in the McGehee transformation.

There are two exceptional orbits producing the dips and peaks at $\varphi\approx 0.6$ and $\varphi\approx 0.8$ in the scattering time. The dip corresponds to an initial conditions on S_T^{eZe} and is thus a triple collision orbit ending in the TCP. Orbits coming from $p_R\ll -P_0$ close to this collision orbit will approach the TCP along the stable manifold S_T^{eZe} and will leave the triple collision region along the unstable manifold U_T^{eZe} into one of the arms leading to single-ionization toward $p_R\gg P_0$. The scattering time has a minimum at that point as the escaping electron leaves with a diverging amount of kinetic energy as one approaches the triple collision orbit; see Fig. 5(b). (Note that it takes an infinite amount of *scaled* time to reach the

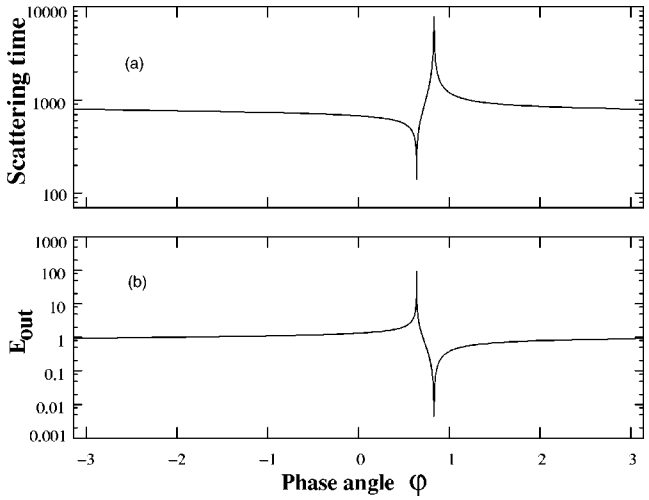

FIG. 5. The scattering time (unscaled) (a) and the energy of the outgoing electron, E_{out}, (b) as a function of the phase angle φ in the collinear *eZe* configuration ($E=0$ and $E_1=1$). Note that the scattering signals are shown on logarithmic scales.

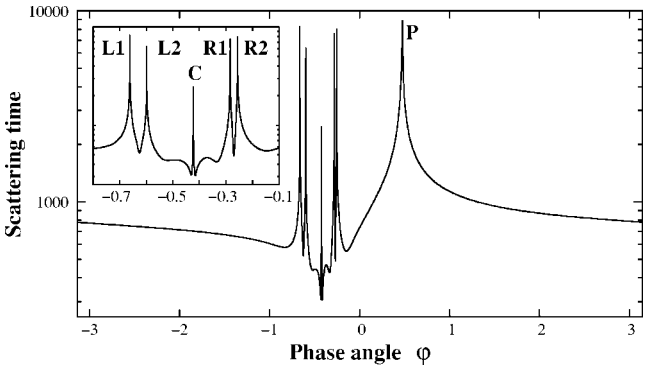

FIG. 6. The scattering time as a function of the phase angle for $E=0$ and $e=0.6$, $\theta_\infty=\pi/2$, and $E_1=-E_2=1$; five distinct peaks appear in the "dip" associated with close encounters with the triple collision point.

TCP fixed point along the S_T^{eZe}, but as $R\to 0$ in this limit, the unscaled momentum p_R becomes singular.)

The peak in the scattering time at $\varphi\approx 0.8$ corresponds to an orbit with initial conditions on the S_D^{eZe} manifold converging to the DEP fixed point and thus leading to double ionisation. Orbits close to the S_D^{eZe} take a large amount of scaled time to pass the DEP which leads to large values of the hyperradius R. These orbits leave the DEP region along the unstable manifold U_D^{eZe} into one of the arms with vanishing unscaled momentum. This leads to the dip in the energy of the outgoing electron in Fig. 5(b) and a diverging scattering time; see Fig. 5(a). The total energy becomes equidistributed between the two electrons for trajectories close to the DEP; the dynamics near the TCP leads, on the other hand, to an unequal partition of the total energy with an infinitely fast outgoing electron and an inner electron bound infinitely deep in the Coulomb singularity at the nucleus.

2. Off-collinear configurations

We will consider off-collinear initial conditions with $\theta_\infty < \pi$ next. Typical scattering signals are very similar to the one described in the previous section for the *eZe* configuration; see, for example, Fig. 6 with $e=0.6$ and $\theta_\infty=\pi/2$. One finds a primary peak P at $\varphi\approx 0.5$ and a dip at $\varphi\approx -0.4$ which contains, however, a set of 5 peaks here. To understand this signal, it is helpful to go back to the PSOS $\theta=\pi$ in Fig. 2. One can identify the peak P with an orbit on the S_D near the S_D^{eZe} approaching the DEP "directly" similar to what one finds in the *eZe* configuration.

New structures emerge in the dip which has in *eZe* been associated with a triple collision orbit on S_T^{eZe}. The TCP fixed point is, however, no longer accessible to off-collinear initial conditions as the stable manifold of the fixed point, S_T, is fully embedded in the *eZe* space; see Table I. Whereas near collision orbits in *eZe* move away from the TCP along the unstable manifold U_T^{eZe}, another route opens up for off-collinear orbits: escape from the TCP along the Wannier ridge which is part of the 3-dimensional unstable manifold U_T. The WR forms in fact a heteroclinic connection between the TCP and DEP and is thus also part of the stable manifold of the DEP, S_D. This and the topology of the phase space leads to the stretching, folding, and cutting mechanism of the S_D discussed in Sec. III B. Orbits coming close to the TCP can thus reach the DEP along the 5 sheets of the 3-dimensional stable manifold S_D giving rise to the 5 peaks in the scattering signal, Fig. 6. The labels $L1$, $L2$, C, $R1$, and $R2$ depicted in the inset of Fig. 6 can indeed be identified with the leaves of the S_D as shown in Fig. 3. The central peak, C, is in particular associated with the part of the S_D directly connected to the Wannier ridge; the outer peaks $L1$, $L2$, $R2$, and $R1$ are related to the folded parts of the S_D and contain orbits which move away from the Wannier ridge after passing the TCP and before reaching the DEP. The difference in the behavior of the orbits in the various leaves becomes obvious when depicting their trajectories in α-$\overline{p}_\alpha$-p_R space as shown in Fig. 7; note that the full orbits are shown here by projecting out the θ dynamics. The center-peak orbit, Fig. 7(a), moves indeed directly from the TCP to the DEP along the WR which is in contrast to for example the $L1$ orbit shown in Fig. 7(b). (Note, that orbits corresponding to the $L2$, $R1$, or $R2$ peak show the same qualitative features as the $L1$ orbit.)

Note that the scattering time diverges at the peaks, both for the peaks in the dip as well as for the primary peak. The corresponding orbits are part of the S_D which is completely embedded in the $\overline{H}=0$ subspace. Orbits on the S_D converge to the DEP and lead thus to double ionisation. The peaks have for $E=0$ no internal structure which reflects the regularity of the dynamics due to the monotonic increase of p_R with time.

We have so far not discussed the θ_∞ dependence on the signal. From Sec. III B, we expect that the peaks move together and converge towards the S_T as one approaches the *eZe* boundary $\theta_\infty\to\pi$, $e\to 1$. This is indeed what one observes, we will come back to this point when discussing scaling laws in Sec. IV C. The other limit towards the *Zee* configuration with $\theta_\infty\to 0$, $e\to 1$ is less obvious; one observes that peaks disappear in pairs consistent with the loop

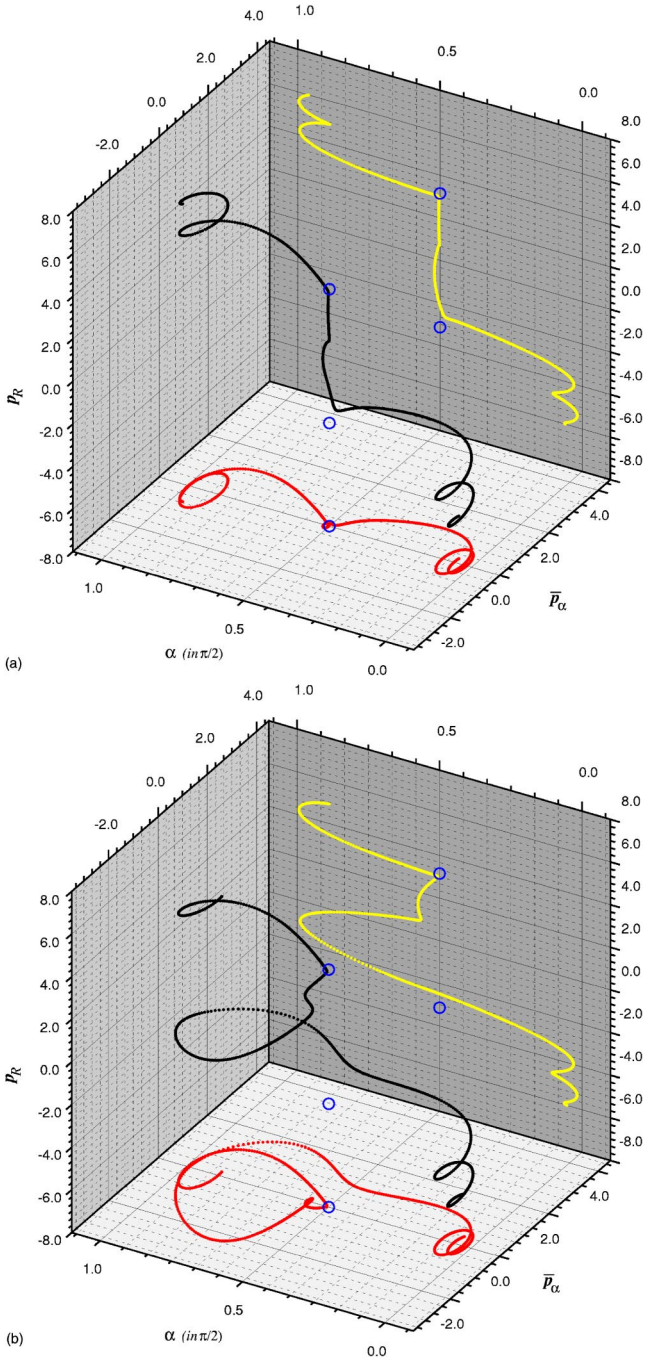

FIG. 7. (Color online) Scattering orbits corresponding to the C peak (a) and the $L1$ peak (b), projected onto the α-$\bar{p}_\alpha$-p_R space. (Note that this is not the PSOS $\theta=\pi$, but the full orbit where the θ dynamics has been projected out.) The initial condition of the orbit are $e=0.6$, $\theta_\infty=\pi/2$, $E_1=1$, $E_2=-1$ with phase angles $\varphi=-0.4256$ in (a) and $\varphi=-0.6612$ in (b) respectively. Projections of the orbit onto the α-$\bar{p}_\alpha$ and α-p_R planes are also shown. The circles represent the positions of the DEP and TCP and their projections.

configuration of the S_D as shown in Fig. 2 until the scattering signal becomes flat for small θ_∞. A detailed analysis of how the near *Zee* dynamics is connected to the rest of the phase space will be presented in [25].

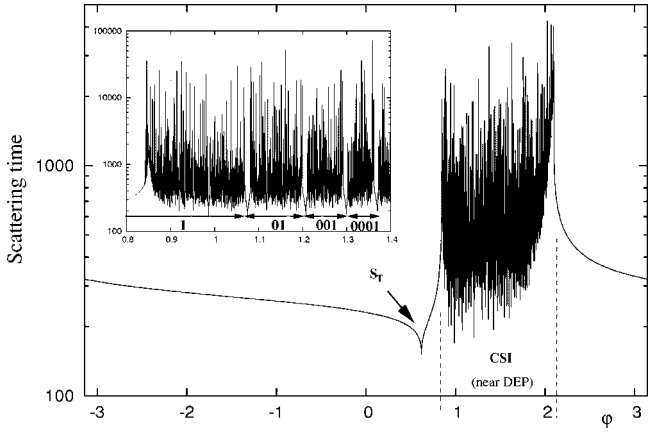

FIG. 8. The time-delay signal for scattering trajectories in the *eZe* subspace ($E_1=0.2$ and $E=-1$). A symbolic dynamics in terms of the symbols {0,1} can be given for this system; the intervals labeled by binary strings refer to initial conditions which have the same symbol code after entering the chaotic scattering region for the number of symbols given.

IV. DYNAMICS FOR $E<0$

We are now ready to venture into the full 5-dimensional phase space $E<0$ with $L=0$; we will approach the problem by analyzing electron scattering signals in a similar way as in the previous section for $E=0$. As mentioned in Sec. II, a smooth transition from $E<0$ towards $\bar{H}=0$ is achieved by taking the limit $E/E_1\to 0$ in the initial conditions, that is, by considering for example $E_1\to\infty$, $E_2\to-\infty$ fixing the total energy at $E=-1$. In this limit, the inner electron is bound infinitely deep in the Coulomb well and interaction between the incoming and bound electrons takes place at $R\to 0$. The dynamics in $\bar{H}=0$ is in this sense equivalent to a dynamics at the triple collision point $R=0$. The smooth transition implies that trajectories close to $\bar{H}=0$ will follow the dynamics in the $E=0$ phase space except near the fixed points where the flow close to the manifold $E=0$ is perpendicular to the invariant subspace $\bar{H}=0$ along the direction p_R; see Eqs. (7) and (14).

A. The *eZe* configuration

We start again with the *eZe* configuration which has been studied extensively in the past [3,6,8,18] and is well understood by now. Figure 8 shows the scattering signal for $E=-1$ and $E_1=0.2$; compared to Fig. 5 for $E=0$, one finds that the peak related to the S_D is replaced by a wildly fluctuating signal typical for chaotic scattering [26]. Note that the dip related to the S_T in $E=0$ is still present.

The dynamics for $E<0$ takes place in the 3-dimensional phase space of Fig. 1(a) where the boundary is given by the $\bar{H}=0$ space. The 2-dimensional stable manifold of the TCP, S_T, is embedded in the 3-dimensional *eZe* space spanned by the 1-dimensional invariant manifolds $S_T^{H\neq 0}$ and S_T^{eZe}; note that only the latter is in the space $\bar{H}=0$; see Table I. The S_T thus intersects the 1-dimensional set of initial conditions for both $E=0$ and $E\neq 0$ independent of E_1. Orbits close to the S_T

manifold approach the triple collision fixed point at $R=0$ and follow the dynamics along the 1-dimensional unstable manifold, U_T^{eZe}, after passing the TCP. The dynamics here is thus similar to the one for $E=0$ as discussed in Sec. III C 1; near collision events lead to ionization of one of the electrons where the ionizing electron escapes with a diverging amount of kinetic energy thus giving rise to the dip in the scattering time.

The behavior of the dynamics near the DEP is linked to the TCP dynamics via time reversal symmetry. The DEP is accessible only via the stable manifold S_D^{eZe} which is embedded in the $E=0$ space; the DEP can thus not be reached for $E<0$ and trajectories can come arbitrary close to the DEP only in the limit $E/E_1 \to 0$. Orbits near the S_D^{eZe} will, however, approach the DEP where they either follow the flow along the unstable direction U_D^{eZe} leading to ionization or follow $U_D^{H\neq 0}$ [or equivalently the Wannier orbit (WO)] into the interior of the *eZe* space; see Fig. 1(a). In the latter case, $\dot{p}_R$ changes sign and electron trajectories fall back towards the nucleus. The particles can now remain trapped for some time in a *chaotic scattering region* located between the TCP and DEP inside the $H=0$ manifold. The DEP thus acts as an entrance gate into this chaotic scattering region. The chaotic scattering interval (CSI) in Fig. 8 replaces the S_D peak in the $E=0$ scattering time signal shown in Fig. 5; it is directly linked to the existence of an entrance gate centered at the DEP fixed point. By time-reversal symmetry, the TCP acts as the exit gate for single electron ionization.

A closer analysis of the strongly fluctuating signal in the CSI reveals the well known binary symbolic dynamics present in the *eZe* configuration [6–8]. Indeed, it is now widely believed (but still not rigorously proved), that the *eZe* configuration behaves like an ideal Smale horseshoe, where the partition leading to a binary symbolic dynamics is provided by the stable and unstable manifold of the triple collision, that is, S_T and U_D. The chaotic signal in the CSI consists of a series of dips flanked by singularities in the delay time on either side, see the magnified region in Fig. 8. The dips correspond to orbits which approach the TCP along the S_T after having entered the chaotic scattering region by coming close to the DEP. Each of these triple collision orbits is embedded in an interval of escaping trajectories, the boundaries of these intervals are given by orbits escaping asymptotically with zero kinetic energy of the outgoing electron. These orbits are thus part of the stable manifold of the asymptotic periodic orbit where one electron stays at infinity with zero kinetic energy. This is in contrast to the case $E=0$ where orbits escaping with zero kinetic energy are part of the stable manifold S_D which leads to double ionization as mentioned in Sec. III C 1.

The shortest chaotic scattering orbits correspond to the widest dip in the CSI (see for example Fig. 8 at $\varphi=1.075$). The corresponding orbit for initial energy $E_1=1000$ is plotted in Fig. 9(a) in $\alpha-\overline{p}_\alpha-p_R$ coordinates. One finds indeed that the orbit approaches the DEP first before turning toward the chaotic scattering region. In this particular case, the orbit stays close to the WO and escapes thus immediately via the exit gate at the TCP. An orbit close to the S_D for $E=0$ is shown in Fig. 9(b) for comparison; this orbit can only escape

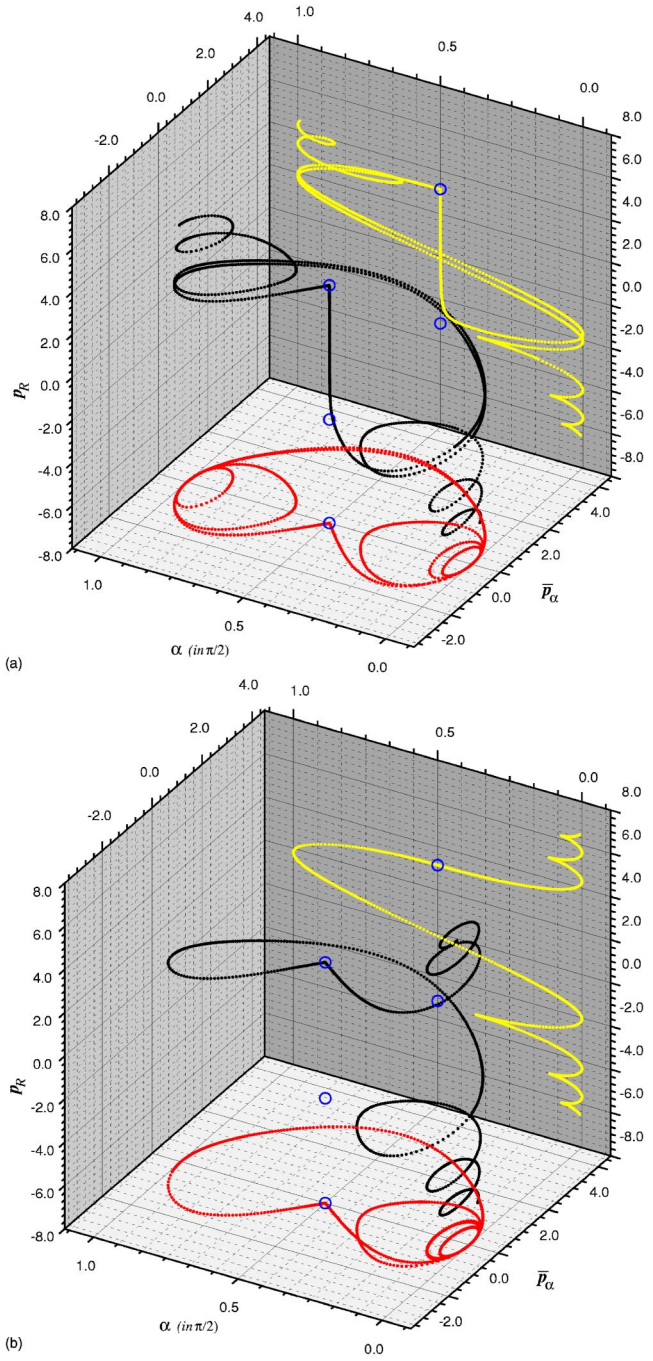

FIG. 9. (Color online) The shortest chaotic scattering orbit in the collinear *eZe* space is plotted in α-$\overline{p}_\alpha$-p_R coordinates for the initial conditions $E/E_1=-0.001$ (a); the corresponding orbit for $E=0$ related to the peak in Fig. 5 is plotted for comparison in (b).

along U_D^{eZe} and chaotic scattering is not possible. Other dips in the CSI are associated with trajectories staying inside the chaotic scattering region for longer times. The intervals between dips can be labeled uniquely by a finite binary code reflecting the order in which binary collisions take place after entering and before escaping the chaotic scattering region. We will not elaborate on the symbolic dynamics here, and refer the interested reader to [6–8]. Note, that the total width

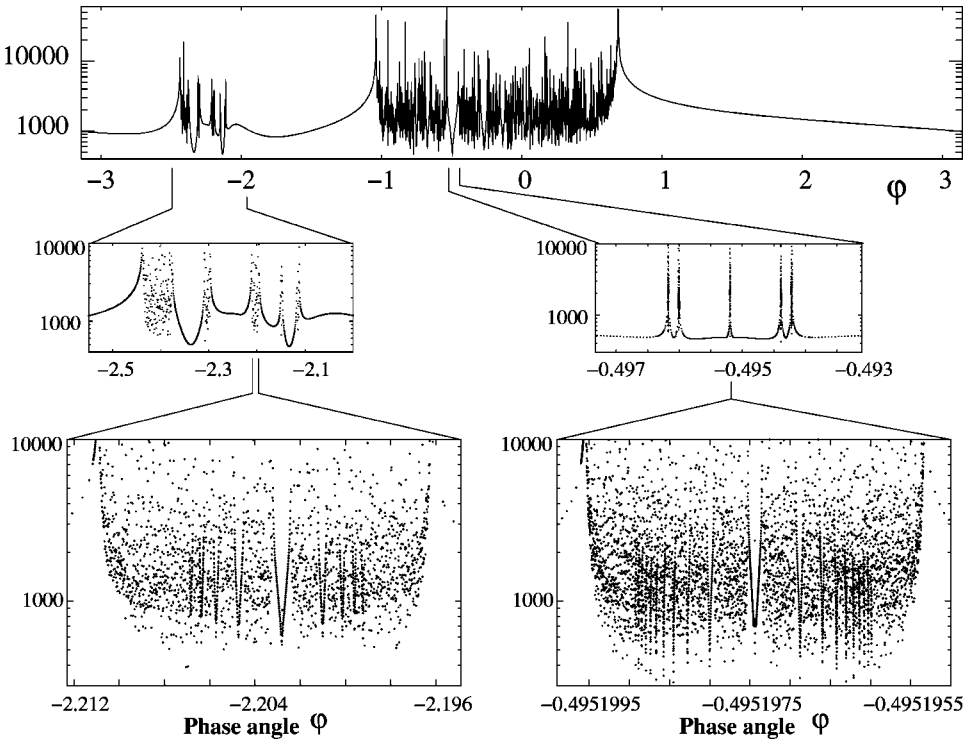

FIG. 10. The scattering time signal for $\theta_\infty=\pi/2$, $e=0.6$, and $E_1=0.2$.

of the chaotic scattering interval reduces to zero in the limit $E/E_1\to 0$, the corresponding scaling law is presented in Sec. IV C.

B. Off-collinear configurations

From the analysis of the dynamics in the $E=0$ phase space and the *eZe* configuration it is now possible to understand the scattering signals for large parts of the $E<0$ phase space by starting from the $E/E_1\to 0$ limit. We note first that the stable and unstable manifolds of the triple collision fixed points which have been so important so far are not contained in the off-collinear $E<0$ phase space; indeed S_D is fully embedded in $E=0$ and S_T is part of the *eZe* phase space; see Table I. The latter implies in particular that triple collisions occur only in the *eZe* configuration. The overall dynamics is, however, clearly influenced by the invariant manifolds of the fixed points. A typical scattering time signal is shown in Fig. 10, here for the scattering parameters $e=0.6$, $\theta_\infty=\pi/2$, $E_1=0.2$, and $E=-1$. It shows a primary dip around $\varphi\approx -2.3$ containing 5 peaks as in the off-collinear scattering data for $E=0$, see Fig. 6, as well as a chaotic scattering interval as in the *eZe* case; see Fig. 8.

In analogy with the *eZe* results, we can identify this primary CSI around $-1.1<\varphi<0.7$ with the "direct" route to the DEP close to the S_D^{eZe}. The DEP and TCP act thus again as the entrance and exit gates, respectively, into or out of a chaotic scattering region. In Fig. 11, we show a sequence of chaotic scattering orbits in configuration space for various E/E_1 belonging to initial conditions in the main dip of the CSI (such as the region around $\varphi\approx -0.495$ in Fig. 10). The trajectories pass the entrance gate near the DEP, but leave the chaotic region immediately again by coming close to the TCP. For small E/E_1, interaction between the two electrons takes place at small values of the hyperradius R and thus close to a $R=E=0$ dynamics; leaving the small R regime into the chaotic scattering region after passing the DEP is for $E/E_1\to 0$ only possible along the Wannier orbit (or equivalently along $U_D^{H\neq 0}$). This can be observed in Fig. 11(d). As

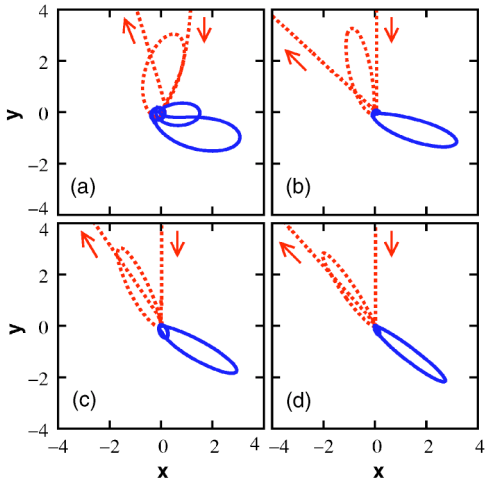

FIG. 11. (Color online) Short chaotic scattering orbits in the *x*-*y* plane with initial conditions in the largest dip in the primary CSI for $E_1=0.2$ (a), 10 (b), 100 (c), and 1000 (d) with fixed total energy $E=-1$. The full lines represent the trajectories of the initially bound electron (with $e=0.6$), the dashed lines correspond to the initially incoming electron (with $\theta_\infty=\pi/2$). The nucleus is at the origin and the direction of the semimajor axis of the initially bound electron is aligned along the *x* axis.

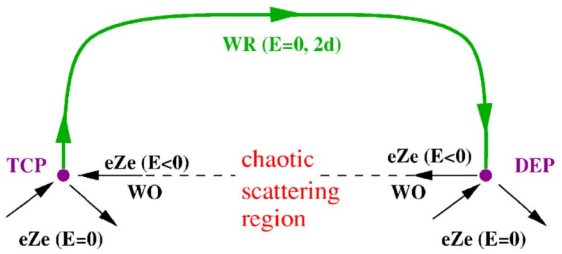

FIG. 12. (Color online) The conveyor belt mechanism: the TCP and DEP fixed points and their heteroclinic connections, the Wannier ridge (WR) for $E=0$ and the Wannier orbit (WO).

E/E_1 increases, the trajectories move away from the WO, but retain the symmetry of the Wannier ridge dynamics. This can be attributed to the fact, that trajectories coming close to the DEP will do so along the Wannier ridge due to the difference in the stability exponents along S_D, that is, $\lambda_{S_D}^{eZe} \ll \lambda_{S_D}^{WR}$; see (13).

In contrast to the scattering signals for the *eZe* configuration, however, new structures appear at the center of the dips in the CSI; see Fig. 10. Indeed, when enlarging the intervals containing the dips, one finds 5 separate peaks similar to those in the primary "dip" at $-2.6<\varphi<-2.0$. In contrast to the $E=0$ case, each of these peaks is in itself a CSI on further magnification. The origin of the 5 peaks is always the same—close encounters with the TCP either via a direct route close to S_T^{eZe} (the primary dip) or when leaving the chaotic scattering region (the primary CSI). The 5 peaks can be related to the folding of the S_D near the TCP as described in Sec. III B. The S_D thus provides a bridge between the TCP and DEP and trajectories can reenter the chaotic scattering region in this way. This leads to the secondary CSI's in each of the 5 peaks; see Fig. 10. Note that the secondary CSI's again show structures very similar to the primary CSI and in fact similar to the CSI in the *eZe* case.

The peaks in the dips suggest that it is possible to create increasingly longer cycles of chaotic scattering events by repeatedly moving from the DEP to the exit channel, the TCP, and then along one of the 5 branches of the stable manifold S_D near the TCP back to the DEP. Indeed, on further magnification of the secondary CSI's, one finds again dips which contain 5 peaks which on further magnification turn out to be CSI's of third order and so on. A whole sequence of self-similar structures emerges in this way where dips give birth to chaotic scattering pattern which in turn have dips containing 5 peaks, etc. The scattering data are thus a macroscopic manifestation of the structure of the dynamics at the triple collision point. They reflect a rather curious dynamical feature, namely a Smale horseshoe, whose entrance and exit points are short-circuited by two different heteroclinic connections between the two fixed points: the Wannier ridge (for $E=0$) leading from the TCP to the DEP and the Wannier orbit connecting the DEP back to the TCP. This gives rise to a *conveyor belt* dynamics as it is schematically sketched in Fig. 12.

The apparent similarities in the CSI signals for both the collinear and off-collinear configurations suggests that the binary symbolic dynamics remains largely intact for a wide range of θ_∞ values. Only the boundaries of the partition which is formed by the S_T itself in the *eZe* case, is modified, turning into channels from which it is possible to reenter the chaotic scattering region. This suggests that the "dips" in each CSI can be labeled by a binary symbol code related to the chaotic dynamics in the chaotic scattering region; from here, trajectories may either escape by coming close to the TCP or may reenter the chaotic scattering region along 5 distinct paths. We thus expect that the dynamics can be well described in terms of $2+5=7$ symbols. However, the existence of such a partition in this high dimensional problem is not obvious and may be the key for explaining the approximate quantum numbers observed in two electron atoms in terms of the classical dynamics.

The analysis so far leaves many questions open. It is in particular a big surprise that the dynamical features found in certain limits, such as the folding of the S_D in $E=0$ space or the existence of a binary symbolic dynamics in the *eZe* configuration, can survive in phase space regions far from these invariant subspaces. Our numerics suggests that the conveyor belt mechanism together with an (approximate) symbolic dynamics works in the whole range $\pi>\theta_\infty>\theta_c\approx\pi/4$ and $1>e>e_c\approx 0.6$ for energy ratios as large as $|E/E_1|=5$. However, there must be a change in the structure of the dynamics eventually. Results obtained in the limiting cases $\theta_\infty=0$—the *Zee* case [4]—or $e=0$ [27] certainly make this a necessity. Especially the transition from *eZe* to *Zee* is of importance in assigning approximate quantum numbers in (quantum) two-electron atoms [5], but remain poorly understood from a classical mechanics point of view. The fact that the conveyor belt is so robust indicates that there are large-scale structures in phase space at work which have not been uncovered so far.

C. Scaling laws

Even though the scope for analytic results is limited in two-electron atom problems, asymptotic scaling laws can be deduced from the linearized dynamics near the fixed points. If the DEP is indeed the sole entrance gate into a chaotic scattering region one would in particular expect universality in the behavior for all CSI's. In the previous sections it has been argued that chaotic scattering trajectories need to come close to the DEP before they can flow out into the chaotic scattering region along the unstable manifold $U_D^{H\neq 0}$. In the limit $E/E_1\to 0$, these trajectories converge towards the $E=0$ manifold and trajectories which will enter the chaotic scattering region along $U_D^{H\neq 0}$ need to come closer and closer to the DEP. The phase space region which eventually enters into chaotic scattering is limited by ejection along the other unstable manifold of the DEP, U_D^{eZe}.

This implies a scaling law for the width Δ_{CSI} of the chaotic scattering intervals for $E/E_1\to 0$ (which should be independent of the prehistory of these trajectory before passing the DEP entrance gate). Let us consider the evolution of a one-dimensional set of initial condition $(-\pi<\varphi\leqslant\pi)$ for small E/E_1 and fixed e and θ_∞. The parts of this segment closest to the S_D come close to the DEP; see Fig. 13. Denote the distance from the 4-dimensional $E=0$ manifold and thus from S_D as δ, that is, we have

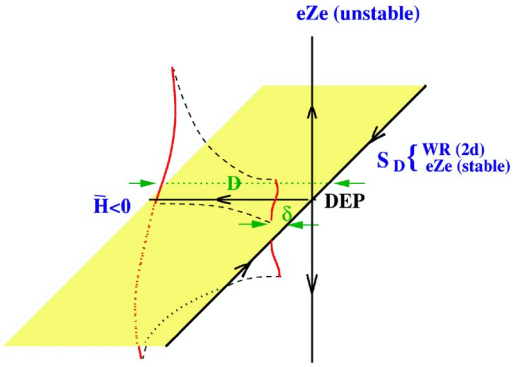

FIG. 13. (Color online) Dynamics near the DEP.

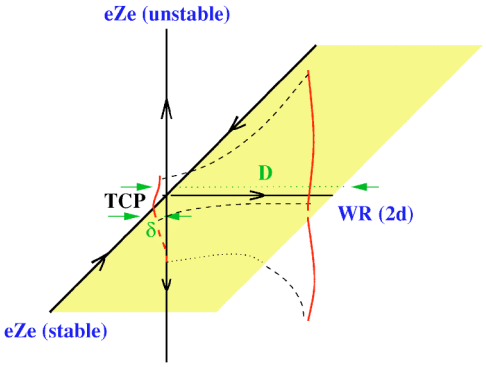

FIG. 15. (Color online) Dynamics near the TCP.

$$\delta \propto |E/E_1|. \tag{15}$$

Chaotic dynamics can be expected only if trajectories reach some distance $D \approx P_0$ from the DEP along $U_D^{\bar{H}\neq 0}$. The time T_D for the segment to get from δ to D is in linear approximation (valid for $E/E_1 \to 0$) of the order

$$T_D \approx \frac{1}{\lambda_{U_D}^{\bar{H}\neq 0}} \ln \frac{D}{\delta}. \tag{16}$$

During that time, intervals of the size Δ_0 on the segment stretch along the U_D^{eZe} direction according to

$$\Delta(T_D) \approx \Delta_0 \exp[\lambda_{U_D}^{eZe} T_D] \approx \Delta_0 (D/\delta)^{\mu}. \tag{17}$$

Here,

$$\mu = \frac{\lambda_{U_D}^{eZe}}{\lambda_{U_D}^{\bar{H}\neq 0}} = \frac{1}{4}\left(\sqrt{\frac{100Z-9}{4Z-1}} - 1\right) \tag{18}$$

is the well known Wannier exponent controlling two-electron ionization processes for $E>0$ [16] and quantum resonance widths [20] near the three particle breakup threshold. The fraction of trajectories entering the chaotic scattering region is thus in the limit $E/E_1 \to 0$ given as $\Delta_{CSI} \propto \Delta_0/\Delta(T_D)$ that is,

$$\Delta_{CSI} \propto (\delta/D)^{\mu} \propto \left|\frac{E}{E_1}\right|^{\mu}, \tag{19}$$

where the energy dependence follows from (15). The scaling law is confirmed by numerical calculations and is indeed universal, that is, it is independent of θ_∞, see Fig. 14(a) (as well as of e, a result not shown here), and is the same for the primary CSI and the CSI's forming the five peaks; see Fig. 14(b). This clearly demonstrates that the DEP is the sole entrance gate into the chaotic scattering region.

In Sec. III C 2, we showed that the 5 peaks in the primary dip are associated with "cutting" the folded S_D at the TCP which leads to 5 distinct paths from the TCP to the DEP; we argued that the center peak C is associated with parts of the S_D manifold directly connected to the Wannier ridge; see Figs. 2 and 3. Trajectories in the C peak thus move along the Wannier ridge, that is, along the U_T^{WR}. The phase space volume which can be transferred from the TCP to the DEP along the Wannier ridge is limited by the flow along the other unstable manifold of the TCP, U_T^{eZe}. This implies an additional scaling law for the width of the center peak Δ_C in the limit $\theta_\infty \to \pi$ as well as $E/E_1 \to 0$ (see Fig. 15): the distance

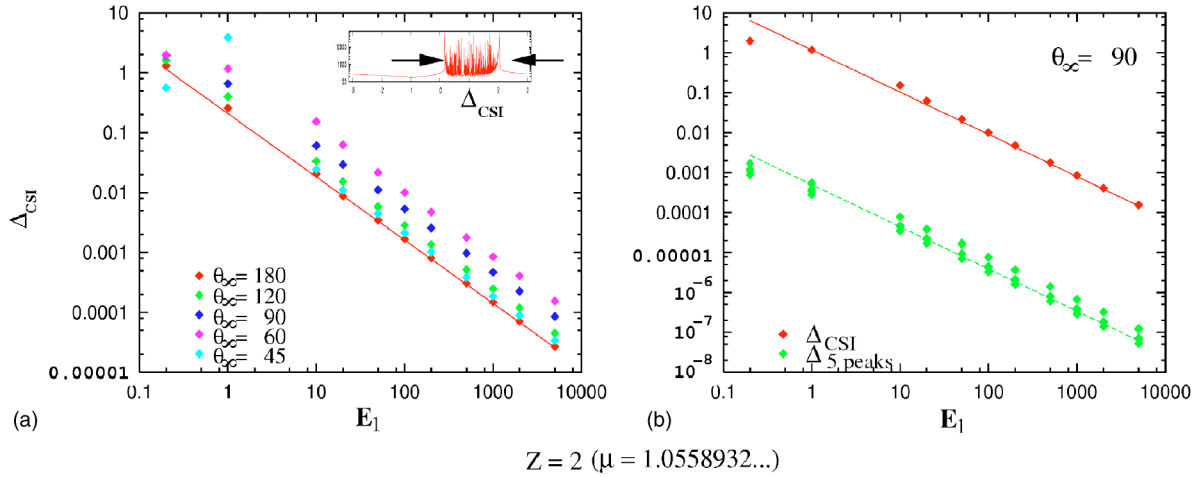

FIG. 14. (Color online) Scaling behavior of the width of the primary CSI for different θ_∞ as well as for the 5 peaks (here for $\theta_\infty = \pi/2$). The other parameters are $e=1$ and $E=-1$.

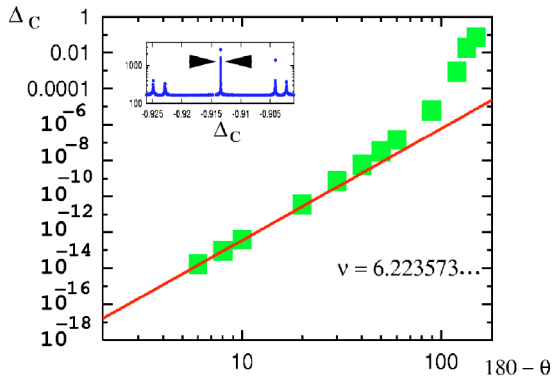

FIG. 16. (Color online) Scaling behavior of the center dip as function of θ_∞, here for $e=1$ and $E/E_1=-0.1$.

of a segment of trajectories from the *eZe* space and thus from the TCP can be measured in terms of $\delta \propto (\pi - \theta_\infty)$. Following a procedure similar to the derivation of (19), one finds that the width of the C peak interval scales as

$$\Delta_C \propto (\pi - \theta_\infty)^\nu |E/E_1|^\mu, \tag{20}$$

with

$$\nu = \frac{\lambda_{U_T}^{eZe}}{\mathrm{Re}[\lambda_{U_T}^{WR}]} = 1 + \sqrt{\frac{100Z-9}{4Z-1}}, \tag{21}$$

and μ given by (18). Note, that the second part of (21) is valid only for $1/4 < Z \leqslant 9/4$; the eigenvalues $\lambda_{U_T}^{WR}$ become real for $Z > 9/4$, in which case the unstable direction with the larger eigenvalue is expected to dominate the behavior along the WR coordinates. Numerical result for the width Δ_C of the center peak in the primary dip are shown in Fig. 16 as a function of $\pi - \theta_\infty$ for fixed $E/E_1=-0.1$ and $e=1$. The agreement with the predicted scaling law demonstrates that the center peak is associated with the path from the TCP to the DEP along the Wannier ridge as described previously.

V. CONCLUSIONS

By using hyperspherical coordinates together with McGehee scaling, it is possible to uncover the structure of the dynamics near the triple collision in detail. We first analyze the dynamics for total energy $E=0$, for which the set of equations of motions is reduced by one. The dynamics is here relatively simple compared to the $E<0$ case due to the monotonic increase in the momentum p_R with respect to the scaled time. The DEP and TCP fixed points are identified as the entrance and exit gate into and out of a chaotic scattering region within the $E<0$ space, respectively. The two fixed points are connected along two different heteroclinic connections, namely the WR for $E=0$ (going from the TCP to the DEP) and the WO for $E<0$ (connecting the DEP back to the TCP). This remarkable effect, which has its origin in the particle exchange symmetry, together with the topology of the phase space leads to the emergence of a 5 leaves structure of the stable manifold of the DEP connected to the stable manifold of the TCP for $p_R < -P_0$. This beautiful effect can be observed in scattering data for both $E=0$ and $E<0$. In the latter case, initial conditions close to the S_D form chaotic scattering intervals (CSI) both for a direct route and for trajectories near the 5 leaves of the S_D; the latter come close to the TCP before entering the chaotic scattering region near the DEP. Scaling laws for the width of the CSI's in the asymptotic limit $E/E_1 \to 0$ and $\theta_\infty \to \pi$ can be derived in terms of the linearized dynamics near the fixed points with scaling exponents given as ratios of stability eigenvalues.

The results described here lay the foundations for a better understanding of the phase space dynamics for the full 5-dimensional phase space $E<0$. That there is a very robust structure becomes apparent when comparing Figs. 8 and 10. The overall signal (neglecting the 5 peaks) remains largely intact which suggests that the complete binary horseshoe spanned by the $S_T^{H\neq 0}$ and the $U_D^{H\neq 0}$ in the *eZe* space is continued into the full phase space. Uncovering this continuation process will be the key in understanding the electron-electron correlation effects giving rise to, for example, the existence of approximate quantum numbers in spectra of two-electron atoms.

ACKNOWLEDGMENTS

We would like to thank the Royal Society (G.T. and N.N.C.), the Hewlett-Packard Laboratories in Bristol (G.T.) and the Korea Research Foundation (KRF-2003-015-C00119) (N.N.C.) for financial support. Numerical support by the KISTI supercomputing center is thankfully acknowledged.

APPENDIX A: NONSINGULAR EQUATIONS OF MOTION

We give here the fully regularized equations of motion in the form of a McGehee regularized version of the 3-body problem with Kustaanheimo-Stiefel (KS) regularized binary collisions. We follow here the treatment in Ref. [8], where the regularisation of the nucleus-electron collisions has been performed by using parabolic coordinates for each electron which are defined by the transformations

$$x_1 = Q_1^2 - Q_2^2, \quad y_1 = 2Q_1Q_2, \quad r_1 = R_1^2 = Q_1^2 + Q_2^2,$$

$$x_2 = Q_3^2 - Q_4^2, \quad y_2 = 2Q_3Q_4, \quad r_2 = R_2^2 = Q_3^2 + Q_4^2,$$

$$p_{x_1} = \frac{Q_1P_1 - Q_2P_2}{2r_1}, \quad p_{y_1} = \frac{Q_2P_1 + Q_1P_2}{2r_1},$$

$$p_{x_2} = \frac{Q_3P_3 - Q_4P_4}{2r_2}, \quad p_{y_2} = \frac{Q_4P_3 + Q_3P_4}{2r_2}, \tag{A1}$$

together with the Kustaanheimo-Stiefel time transformation [23,24]

$$dt = r_1 r_2 d\tau. \tag{A2}$$

Here, (x_i, y_i) and (p_{x_i}, p_{y_i}) are the position and momentum in Cartesian coordinates of electron $i=1,2$ moving in the plane. The notations **Q** and **P** will be used for (Q_1, Q_2, Q_3, Q_4) and

(P_1, P_2, P_3, P_4), respectively. The regularized Hamiltonian G can now be written as

$$\begin{aligned} G &= r_1 r_2 (H - E) \\ &= \frac{1}{8} r_2 (P_1^2 + P_2^2) + \frac{1}{8} r_1 (P_3^2 + P_4^2) - Z r_2 - Z r_1 \\ &\quad + r_1 r_2 \left(-E + \frac{1}{r_{12}} \right), \end{aligned} \tag{A3}$$

where the electron-electron distance r_{12} is

$$r_{12} = [(Q_1^2 + Q_2^2)^2 + (Q_3^2 + Q_4^2)^2 - 2(Q_1 Q_3 + Q_2 Q_4)^2 + 2(Q_1 Q_4 - Q_2 Q_3)^2]^{1/2}. \tag{A4}$$

The Hamilton's equations of motion,

$$\frac{d\mathbf{Q}}{d\tau} = \frac{\partial G}{\partial \mathbf{P}}, \quad \frac{d\mathbf{P}}{d\tau} = -\frac{\partial G}{\partial \mathbf{Q}}, \tag{A5}$$

are now given as

$$\frac{dQ_1}{d\tau} = \frac{1}{4} r_2 P_1, \quad \frac{dQ_2}{d\tau} = \frac{1}{4} r_2 P_2, \quad \frac{dQ_3}{d\tau} = \frac{1}{4} r_1 P_3, \quad \frac{dQ_4}{d\tau} = \frac{1}{4} r_1 P_4, \tag{A6}$$

and

$$\begin{aligned} \frac{dP_1}{d\tau} &= -\left\{ \frac{1}{4} Q_1 (P_3^2 + P_4^2) - 2ZQ_1 + 2Q_1 r_2 \left(-E + \frac{1}{r_{12}} \right) \right. \\ &\quad \left. - 2\frac{r_1 r_2}{r_{12}^3} [r_1 Q_1 + (Q_4^2 - Q_3^2) Q_1 - 2Q_2 Q_3 Q_4] \right\}, \\ \frac{dP_2}{d\tau} &= -\left\{ \frac{1}{4} Q_2 (P_3^2 + P_4^2) - 2ZQ_2 + 2Q_2 r_2 \left(-E + \frac{1}{r_{12}} \right) \right. \\ &\quad \left. - 2\frac{r_1 r_2}{r_{12}^3} [r_1 Q_2 - (Q_4^2 - Q_3^2) Q_2 - 2Q_1 Q_3 Q_4] \right\}, \\ \frac{dP_3}{d\tau} &= -\left\{ \frac{1}{4} Q_3 (P_1^2 + P_2^2) - 2ZQ_3 + 2Q_3 r_1 \left(-E + \frac{1}{r_{12}} \right) \right. \\ &\quad \left. - 2\frac{r_1 r_2}{r_{12}^3} [r_2 Q_3 + (Q_2^2 - Q_1^2) Q_3 - 2Q_1 Q_2 Q_4] \right\}, \\ \frac{dP_4}{d\tau} &= -\left\{ \frac{1}{4} Q_4 (P_1^2 + P_2^2) - 2ZQ_4 + 2Q_4 r_1 \left(-E + \frac{1}{r_{12}} \right) \right. \\ &\quad \left. - 2\frac{r_1 r_2}{r_{12}^3} [r_2 Q_4 - (Q_2^2 - Q_1^2) Q_4 - 2Q_1 Q_2 Q_3] \right\}. \end{aligned} \tag{A7}$$

Singular behavior may occur at the triple collision and thus in terms containing $1/r_{12}$ in (A7); it turns out, however, that the KS-time transformation (A2) also lifts the triple collision singularity from the equations of motion: $r_{12}=0$ can indeed only occur if $r_1=r_2=0$ due to the *e*-*e* repulsion. Terms containing $1/r_{12}$ in (A7) indeed vanish proportional to $\sqrt{R}$ when $r_{12} \to 0$ where the hyperradius R in the new coordinates takes on the form

$$R = \sqrt{(Q_1^2 + Q_2^2)^2 + (Q_3^2 + Q_4^2)^2}. \tag{A8}$$

It is, however, still advantageous to employ McGehee scaling as introduced in Sec. II in addition to a KS transformation. By defining

$$\overline{\mathbf{Q}} = \frac{\mathbf{Q}}{\sqrt{R}}, \tag{A9}$$

one arrives at a set of coordinates where the $\overline{\mathbf{Q}}$ and $\overline{r_{12}}$ can take on nonzero values at the triple collision. (One can actually show that $\overline{r_{12}} > 0$ everywhere for $E \leqslant 0$, for example $\overline{r_{12}} > 0.156\ldots$ for $Z=2$.) This means in particular that expressions containing r_{12} in (A7) remain in general finite in the McGehee-scaled coordinates even at the triple collision. For numerical calculations, it is thus more convenient to use the scaled coordinates which are less sensitive to numerical errors due to small denominators.

After introducing the additional time transformation

$$d\overline{\tau} = \sqrt{R} d\tau \tag{A10}$$

(which leads to a speedup near the triple collision compared to using KS-time transformation only), one obtains the equations of motion for the scaled coordinates $\overline{\mathbf{Q}}$ as

$$\begin{aligned} \frac{d\overline{Q_1}}{d\overline{\tau}} &= \frac{1}{4} \overline{r_2} \overline{P_1} - \frac{1}{2} \overline{Q_1} \overline{r_1 r_2 p_R}, \\ \frac{d\overline{Q_2}}{d\overline{\tau}} &= \frac{1}{4} \overline{r_2} \overline{P_2} - \frac{1}{2} \overline{Q_2} \overline{r_1 r_2 p_R}, \\ \frac{d\overline{Q_3}}{d\overline{\tau}} &= \frac{1}{4} \overline{r_1} \overline{P_3} - \frac{1}{2} \overline{Q_3} \overline{r_1 r_2 p_R}, \\ \frac{d\overline{Q_4}}{d\overline{\tau}} &= \frac{1}{4} \overline{r_1} \overline{P_4} - \frac{1}{2} \overline{Q_4} \overline{r_1 r_2 p_R}, \end{aligned} \tag{A11}$$

with

$$\overline{\mathbf{P}} = \mathbf{P}, \tag{A12}$$

and $\overline{p_R}$ is the scaled momentum of the hyperradius as in (6); it can be expressed in terms of the scaled parabolic coordinates as

$$\overline{p_R} = \frac{1}{2} (\overline{Q_1} \overline{P_1} + \overline{Q_2} \overline{P_2} + \overline{Q_3} \overline{P_3} + \overline{Q_4} \overline{P_4}). \tag{A13}$$

The equations of motion for $\overline{\mathbf{P}}$ are the same as in (A7) where the variables $\mathbf{Q}$, $\mathbf{P}$, τ and the energy E are replaced by the scaled variables; the scaled energy $\overline{E}$ is as in (6) given by

$$\overline{E} = RE \quad \text{with} \quad \frac{d\overline{E}}{d\overline{\tau}} = \overline{r_1 r_2 p_R} \overline{E}. \tag{A14}$$

The full set of equations of motion (A7), (A11), and (A14)

are free of singularities and are numerically stable both in the vicinity of binary and triple collisions.

APPENDIX B: POINCARÉ SURFACE OF SECTION

A "good" global Poincaré surface of section (PSOS) should fulfill two basic ingredients, namely (i) almost all trajectories cross the PSOS and (ii) the vector field is transversal to the PSOS (except on lower dimensional invariant manifolds). The latter condition is readily fulfilled for the PSOS $\theta=\pi$ as

$$\dot{\theta}=\frac{p_\theta}{\sin^2\alpha\cos^2\alpha}\neq 0$$

for all points on the PSOS except those in the invariant *eZe* space with $\theta=\pi$ and $p_\theta=0$.

Next, we show that a generic orbit with total angular momentum $L=0$ intersects the hypersurface $\theta=\pi$ in all three energy regimes $E=0,\pm 1$ at least once. Let us assume that there are trajectories which never intersect $\theta=\pi$ for all times. A possible way for this to happen is, that trajectories oscillate in the range $\theta\in[-\pi,\pi]$ without crossing the PSOS. This means, there must be turning points of the forms A and B in Fig. 17, where $p_\theta=0$ with $-\pi<\theta<\pi$. However, employing (7), we have at such a point

$$\dot{p}_\theta=\frac{\sin 2\alpha\sin\theta}{2[1-\sin 2\alpha\cos\theta]^{3/2}}\begin{cases}<0 & \text{for } -\pi<\theta<0 \text{ (B)},\\ >0 & \text{for } 0<\theta<\pi \text{ (A)},\end{cases} \tag{B1}$$

whereas we would need $\dot{p}_\theta<0$ in scenario A and $\dot{p}_\theta>0$ in B. These cases can thus be excluded.

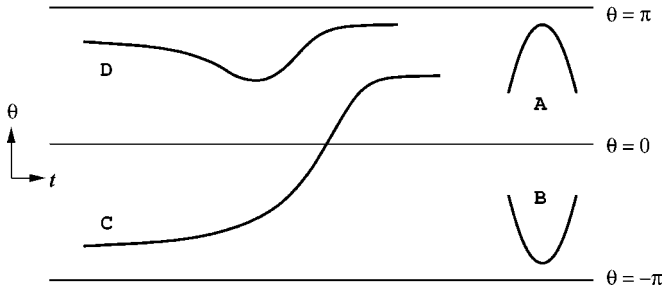

FIG. 17. Impossible trajectories.

The other possibility is that there exist trajectories which never cross the PSOS by converging to a fixed value in θ with $\theta\neq 0$ or π and thus $p_\theta\to 0$ for $t\to\pm\infty$ as indicated by the cases C and D in Fig. 17. (Orbits converging towards $\theta=0$ or π must lie at homoclinic or heteroclinic intersections of the stable and unstable manifolds of the invariant *Zee* or *eZe* subspaces and are thus of measure zero in the full phase space.) If convergence in θ occurs for $t\to\pm\infty$, this implies $\dot{p}_\theta\to 0$ and thus $\alpha\to 0$ or $\pi/2$ in these limits; see (B1). Furthermore, from Eq. (5) we have $p_\theta=p_{\theta_1}=-p_{\theta_2}\to 0$, that is, both electrons have angular momentum zero asymptotically. This is possible only if $\theta=0$ or π or if one of the two electrons escapes to infinity. The final state must thus be an incoming and outgoing scattering trajectory of the type shown in Fig. 4 with $\epsilon=1$. However, for finite α, the electron-electron interaction will push the inner electron onto an elliptic motion around the nucleus and θ will thus cross $\theta=\pi$. This gives the contradiction and there are no trajectories of the form C and D as depicted in Fig. 17. Consequently the hypersurface $\theta=\pi$ is a suitable Poincaré surface of section for all energies.

[1] F. Diacu and P. Holmes, *Celestial Encounters: The Origins of Chaos and Stability* (Princeton University Press, Princeton, NJ, 1997).
[2] M. C. Gutzwiller, *Chaos in Classical and Quantum Mechanics* (Springer, New York, 1990).
[3] G. S. Ezra, K. Richter, G. Tanner, and D. Wintgen, J. Phys. B **24**, L413 (1991).
[4] K. Richter and D. Wintgen, Phys. Rev. Lett. **65**, 1965 (1990).
[5] G. Tanner, K. Richter, and J. M. Rost, Rev. Mod. Phys. **72**, 497 (2000).
[6] Z.-Q. Bai, Y. Gu, and J. M. Yuan, Physica D **118**, 17 (1998).
[7] M. M. Sano, J. Phys. A **37**, 803 (2004).
[8] K. Richter, G. Tanner, and D. Wintgen, Phys. Rev. A **48**, 4182 (1993).
[9] B. Duan, Z.-Q. Bai, and Y. Gu, Phys. Rev. A **61**, 062711 (2000).
[10] P. V. Grujic and N. S. Simonović, J. Phys. B **28**, 1159 (1995).
[11] T. Yamamoto and K. Kaneko, Prog. Theor. Phys. **100**, 1089 (1998); Phys. Rev. Lett. **70**, 1928 (1993).
[12] D. A. Herrick, Adv. Chem. Phys. **52**, 1 (1983).
[13] A. Bürgers, D. Wintgen, and J.-M. Rost, J. Phys. B **28**, 3163 (1995).
[14] J. M. Feagin and J. S. Briggs, Phys. Rev. Lett. **57**, 984 (1986).
[15] N. N. Choi, M.-H. Lee, and G. Tanner, Phys. Rev. Lett. **93**, 054302 (2004).
[16] G. H. Wannier, Phys. Rev. **90**, 817 (1953).
[17] L. A. Pars, *A Treatise on Analytical Dynamics* (Wiley, New York, 1965), p. 575.
[18] J. M. Rost, Phys. Rep. **297**, 271 (1998).
[19] R. McGehee, Invent. Math. **27**, 191 (1974).
[20] J. M. Rost and D. Wintgen, Europhys. Lett. **35**, 19 (1996).
[21] K. Richter and D. Wintgen, J. Phys. B **23**, L197 (1990).
[22] F. Diacu, S. Kaplan, and C. Stoica, "On the stability of the Helium atom," report.
[23] P. Kustaanheimo and E. Stiefel, C. R. Hebd. Seances Acad. Sci. **260**, 805 (1965).
[24] S. J. Aarseth and K. Zare, Celest. Mech. **10**, 185 (1974).
[25] N. N. Choi, M.-H. Lee, and G. Tanner (in preparation).
[26] P. Gaspard, *Chaos, Scattering and Statistical Mechanics* (Cambridge University Press, Cambridge, England, 1998).
[27] Y. Gu and J.-M. Yuan, Phys. Rev. A **47**, R2442 (1993).